

See discussions, stats, and author profiles for this publication at: <https://www.researchgate.net/publication/263276580>

Breakup of a viscous poorly conducting liquid thread subject to a radial electric field at zero Reynolds number

Article in *Physics of Fluids* · October 2012

DOI: 10.1063/1.4757388

CITATIONS

18

READS

57

1 author:



Qiming Wang

New Jersey Institute of Technology

16 PUBLICATIONS **147** CITATIONS

[SEE PROFILE](#)

Some of the authors of this publication are also working on these related projects:



Macroscale model of electrified liquid thread [View project](#)

Breakup of a poorly conducting liquid thread subject to a radial electric field at zero Reynolds number

Qiming Wang

Citation: *Phys. Fluids* **24**, 102102 (2012); doi: 10.1063/1.4757388

View online: <http://dx.doi.org/10.1063/1.4757388>

View Table of Contents: <http://pof.aip.org/resource/1/PHFLE6/v24/i10>

Published by the [American Institute of Physics](#).

Related Articles

Barriers to front propagation in ordered and disordered vortex flows
Chaos **22**, 037103 (2012)

Micro-manipulation using rotational fluid flows induced by remote magnetic micro-manipulators
J. Appl. Phys. **112**, 064912 (2012)

Instrument for layer-by-layer deposition of catalyst layers directly on proton exchange membrane for direct methanol fuel cell
Rev. Sci. Instrum. **83**, 095005 (2012)

Dielectric-solid polarization at strong fields: Breakdown of Smoluchowski's electrophoresis formula
Phys. Fluids **24**, 082005 (2012)

Scalar transport and perturbation dynamics in intermittent magnetohydrodynamic flow
Phys. Fluids **24**, 084104 (2012)

Additional information on Phys. Fluids

Journal Homepage: <http://pof.aip.org/>

Journal Information: http://pof.aip.org/about/about_the_journal

Top downloads: http://pof.aip.org/features/most_downloaded

Information for Authors: <http://pof.aip.org/authors>

ADVERTISEMENT



**Running in Circles Looking
for the Best Science Job?**

Search hundreds of exciting
new jobs each month!

<http://careers.physicstoday.org/jobs>

physicstodayJOBS



Breakup of a poorly conducting liquid thread subject to a radial electric field at zero Reynolds number

Qiming Wang^{a)}

*Department of Mathematical Sciences, New Jersey Institute of Technology,
New Jersey 07102, USA*

(Received 12 March 2012; accepted 11 September 2012; published online 8 October 2012)

We study the breakup of an axisymmetric viscous liquid thread with finite conductivity immersed in another viscous fluid, which are confined to a concentrically placed cylindrical electrode that is held at a constant voltage potential. The annular fluid between the core thread and the electrode is assumed to be insulating. The flow then is driven by a radial electric field together with capillary and viscous forces. A linear stability analysis is carried out when the perturbation on the thread interface is small and nonlinear evolution and satellite drop formation near pinch-off are investigated by direct numerical simulations based on boundary integral method. The numerical results reveal that satellite formation as well as breakup time is affected significantly when the effect of charge convection is important compared with electric conduction. For large conduction, the evolutions of the thread are close to those obtained for a perfectly conducting core fluid. Finally, we show numerically that the local dynamics may be altered when the conduction is weak compared to the perfect conductor limit. New scalings near breakup are obtained from a long wave model. © 2012 American Institute of Physics. [<http://dx.doi.org/10.1063/1.4757388>]

I. INTRODUCTION

In the absence of electric fields, the dynamics of uncharged liquid threads has been studied extensively. Linear theory reveals that the thread is unstable subject to a long wave perturbation.^{1,2} The liquid thread evolves into nonlinear regime eventually, which can only be tracked by numerical simulations. It is observed that a series of small droplets forms as the interface thins to rupture, which leads to a finite-time singularity. Further study on local dynamics of jet breakup was first performed by Refs. 3 and 4 on a Navier Stokes jet and Ref. 5 on a Stokes jet, respectively, where self similar solutions are constructed analytically. Numerical evidence of self-similar pinching solution on inviscid and two phase Stokes flows was shown by Refs. 6 and 7, for example. An extensive review of jet dynamics and breakup can be found in Ref. 8 and the references therein.

The stability and dynamics of an electrified jet is more complicated, where either an axial or radial electric field can be applied. For axial electric fields, linear theory was derived in early studies, for example, in Refs. 9 and 10, showing a stabilizing effect of axial electric fields, which would lead to a long formation of jet. The effect of charge relaxation at jet surface was discussed for different viscosity regimes in Ref. 11. Recently, an asymptotic model assuming a slender fluid jet is studied in the axial field case in Ref. 12, where both axisymmetric and sinuous modes are considered and good agreement with the full linear theory is obtained. When a radial electric field is applied, the linear stability analysis for perfectly conducting jets has been carried out in Refs. 13 and 14, where long (short) waves are shown to be stabilized (destabilized). The stability of a poorly conducting jet was studied¹⁵ using a leaky dielectric model (see Refs. 16 and 17) in axisymmetric configuration, which showed electric conduction and relative permittivity affects the growth rate and the most unstable modes, even though the perfect conductor limit provides a good approximation

^{a)}qw6@ubc.math.ca. Present address: Department of Mathematics, University of British Columbia, V6T 1Z2 BC, Canada.

under some circumstances. A discussion on the validity of slender jet model is also carried out there. Furthermore, the temporal linear stability analysis of a charged coflowing jet with two immiscible viscous fluids in radial electric fields was considered in Ref. 18 with also a leaky dielectric model. It is shown that low conductivity/relative permittivity will reduce growth rate when the viscosity is moderate, while the influence is small when the jet is nearly inviscid, in which case electric shear stresses at the interface cannot be balanced and hence the jet behaves like a perfect conductor. Numerical investigation on the problem of a Newtonian viscous perfectly conducting thread in radial electric fields was studied by Refs. 19 and 20 using a one-dimensional approximation, by Ref. 21 using both 1D and 2D simulations and by Refs. 22 and 23 using boundary integral method for a single inviscid jet and two phase Stokes flow inside a cylindrical electrode, respectively. The results reveal a larger (volume) satellite drop formation when the field is applied radially. Meanwhile the main drops are observed to be elongated radially in the direction of applied field and the breakup is in general retarded. In addition, López-Herrera *et al.*²⁴ studied the problem experimentally on the influence of viscosity and electric field strength on the breakup dynamics. Good agreement is obtained by comparing with one dimensional results when the electric field is not too large, assuming the electrode is sufficiently far away from the liquid interface initially. Sufficiently large field, on the other hand, usually leads to nonaxisymmetric instability. When the interface position is sufficiently close to the electrode initially, pinching may be suppressed and fluid would tend to touch the outer electrode (tube wall) due to the electrostatic attraction.^{20,23} Furthermore, electrokinetic effect should be taken into account when the surface ion is present at interface or an electric double layer can be identified near the electrode. The linear theory for such a setting was first discussed in Ref. 25 for a thin annular electrolyte film and a general model on electrohydrodynamics was reviewed in Ref. 17. Recently, Conroy *et al.*²⁶ studied the nonlinear dynamics of a thin annular electrolyte film attached to the interior of a cylindrical electrode which extends the electrostatic model in Ref. 23. The two studies both show a finite-time singularity (wall touch down solution) for the sharp rupture compared to the infinite-time singularity studied in Refs. 27 and 28 for pure capillary film drainage. A non-uniform steady state solution is also obtained in Ref. 26 where the Debye length is small relatively to the undisturbed film thickness. A slender electrolytic jet with hydrodynamically passive surrounding fluid is considered recently in Ref. 29, where pinching solution and satellite formation are analyzed by showing extensive numerical results, which shows dynamics can be modified in a number of ways that depends on different electric parameters. But the local dynamics is shown to remain the same as non-electrified case and is described by a self similar solution. The problem is complicated due to the richness of parameters.

However, apart from the reduced asymptotic model, few studies have been done to discuss the role of finite conduction on nonlinear dynamics of the full axisymmetric problem, when a radial electric field is applied. In this paper, we aim to investigate the situations for a poorly conducting thread immersed in another viscous fluid using a leaky dielectric model. We first extend the linear stability analysis in Ref. 15 to include a second fluid surrounding the liquid thread at zero Reynolds number. Similar to the findings in Ref. 15, the dominant modes for long waves switch trend (in our case, from order one to a quadratic trend) for a single thread. However, this switching behavior disappears once a second fluid is added. In general, the growth rate, as described in Ref. 15, is reduced by decreasing conductivity/permittivity of the core fluid. But the growth rate changes little when two fluids are comparably viscous, hence little information is delivered on how imperfect electric conductivity and permittivity influences the dynamics of two phase system in this case. We address this by performing a direct simulation. The derived linear theory is also used to valid our code later. Then we show the nonlinear evolutions of the system is significantly affected by differing these electric parameters even the linear theory shows little change when both two fluids are highly viscous. In particular, breakup time and interface shape are dependent on those electric parameter values. We do the simulation by using a boundary integral method to simulate both electrostatic and Stokes flow problems, which extends the study in Ref. 23 where only perfect conductor limit is considered. In current study, we only report the results for equal viscosity ratio, $\lambda = 1$. Near breakup, satellite formation differs when the surface charge convection becomes important. It is noticed that even in the case of a radial electric field, significant shear stresses are produced when conductivity (relative permittivity) is small or moderate. Those shearing forces must be responsible

for the various interface shapes at pinching. In these cases, local pinching dynamics might be altered, since we show numerically that the electric force becomes important compared to capillary force in the necking region. We finally comment that a long wave model which retains annular viscous fluid that is much less viscous than the core gives new scalings on pinching. To see this from full problem, a more robust and sophisticated code is needed and hence left for future investigation.

The rest of the paper is organized as follows. The equations utilizing a leaky dielectric model are introduced in Sec. II. Full linear theory for the axisymmetric problem with arbitrary viscosity ratio is derived and studied in Sec. III. Section IV presents the numerical method based on boundary integral techniques. The numerical solutions are discussed in Sec. V, and finally, concluding remarks are given in Sec. VI.

II. MATHEMATICAL FORMULATION

We consider the dynamics of a viscous incompressible two-fluid system arranged in a core-annular configuration inside a cylindrical tube of constant circular cross section of radius b . Cylindrical polar coordinates $\mathbf{x} = r\mathbf{e}_r + z\mathbf{e}_z$ are used with the z -axis along the pipe axis. A schematic of the problem is provided in Figure 1. Fluid 1 occupies the core region defined by $0 < r < S(z, t)$, while fluid 2 occupies $S(z, t) < r < b$, where we have assumed axisymmetry (all variables are independent of the azimuthal angle). In what follows the effect of gravity is neglected which is a good approximation when the ratio of gravitational to capillary forces is small (see Ref. 27). A potential difference V_0 is applied between the liquid thread and the cylindrical tube (outer electrode) at the beginning. In the unperturbed state, surface charge density at the interface is created by the radial field, with the liquid bulk being electrically neutral. We define the electric field by $\mathbf{E}_i = -\nabla\phi_i$ where $\phi_i(r, z, t)$ is the voltage potentials in region i .

A. The electric field

Laplace's equation is satisfied in both regions

$$\nabla^2\phi_i = 0 \quad \text{or} \quad \nabla \cdot \mathbf{E}_i = 0, \quad i = 1, 2 \quad (1)$$

with constant potential boundary condition on the outer electrode $r = b$, $\phi_2(b, z, t) = 0$ (assuming the electrode is grounded without loss of generality).

On the interface $r = S(z, t)$,

$$\phi_1 = \phi_2, \quad \text{i.e.,} \quad \mathbf{t} \cdot \mathbf{E}_1 = \mathbf{t} \cdot \mathbf{E}_2, \quad (2)$$

$$\epsilon_2 \mathbf{n} \cdot \mathbf{E}_2 - \epsilon_1 \mathbf{n} \cdot \mathbf{E}_1 = \frac{q}{\epsilon_0}, \quad (3)$$

where \mathbf{t} and \mathbf{n} denote unit tangential and normal vector, respectively; ϵ_i is the dielectric constant in two phases and q is surface charge density, which is determined by the following equation:

$$q_t + \mathbf{u}_s \cdot \nabla_s q - q \mathbf{n} \cdot (\mathbf{n} \cdot \nabla) \mathbf{u}_s = \sigma_1 \mathbf{E}_{1n} - \sigma_2 \mathbf{E}_{2n}, \quad (4)$$

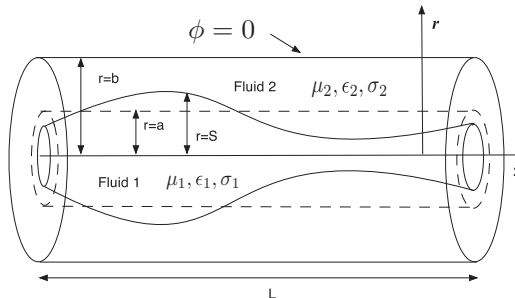


FIG. 1. Schematic of the problem geometry.

where $\mathbf{E}_{in} = -\mathbf{n} \cdot \nabla \phi_i$, σ_i is the conductivity of phase i and subscript s denotes the surface evaluation. For the rest of study we would further assume the annular fluid to be insulating, namely, zero conductivity, $\sigma_2 = 0$.

B. Fluid motion in the presence of electric field

In the zero Reynolds number limit the flow in regions 1 and 2 is governed by the Stokes equations:

$$-\nabla p_i + \mu_i \nabla^2 \mathbf{u}_i = 0, \quad \nabla \cdot \mathbf{u}_i = 0, \quad i = 1, 2, \quad (5)$$

where $\mathbf{u}_i = u_i \mathbf{e}_r + w_i \mathbf{e}_z$ is the fluid velocity, p_i is the pressure, and μ_i is the fluid viscosity in each phase. The no-slip and no-penetration boundary condition at the wall requires

$$u_2(b, z, t) = w_2(b, z, t) = 0. \quad (6)$$

It remains to prescribe all other boundary conditions on the moving interface $r = S(z, t)$. These are the usual kinematic condition

$$u_i = S_t + w_i S_z, \quad \text{on } r = S(z, t), \quad (7)$$

and the tangential and normal stress balances

$$[\mathbf{t} \cdot \mathcal{T} \cdot \mathbf{n}]_2^1 = 0, \quad (8)$$

$$[\mathbf{n} \cdot \mathcal{T} \cdot \mathbf{n}]_2^1 = -\gamma \kappa, \quad (9)$$

where $\mathbf{t} = (S_z \mathbf{e}_r + \mathbf{e}_z)/(1 + S_z^2)^{1/2}$ and $\mathbf{n} = (\mathbf{e}_r - S_z \mathbf{e}_z)/(1 + S_z^2)^{1/2}$ are the unit tangent and normal (pointing into region 2) at any point on the interface, κ is the curvature at that point, γ is the surface tension assumed to be constant and the notation $[\cdot]_2^1$ denotes a jump in a quantity as the interface is crossed from the core to the annulus. The stress tensor \mathcal{T} has hydrodynamic and electrostatic (Maxwell stress) contributions which we write as $\mathcal{T} = \boldsymbol{\sigma} - \mathcal{M}$, where

$$\boldsymbol{\sigma} = -p\mathbf{I} + \mu(\nabla \mathbf{u} + \nabla \mathbf{u}^T), \quad \mathcal{M} = \epsilon_i \epsilon_0 (\mathbf{E}\mathbf{E} - \frac{1}{2} \mathbf{I} |\mathbf{E}|^2), \quad (10)$$

with \mathbf{I} denoting the identity matrix and ϵ_i the electrical permittivity of fluid i (the permittivity of free space is $\epsilon_0 \approx 8.8542 \times 10^{-12}$ F/m). Specifically, the discontinuity of the electric field across the interface causes a jump of stress $[\mathcal{M} \cdot \mathbf{n}]_2^1$ given by

$$\Delta \mathbf{f}^e = \frac{\epsilon_2 \epsilon_0}{2} \left(\left[\mathbf{E}_{2n}^2 - \frac{\epsilon_1}{\epsilon_2} \mathbf{E}_{1n}^2 - \left(1 - \frac{\epsilon_1}{\epsilon_2}\right) \mathbf{E}_t^2 \right] \mathbf{n} + 2 \left(\mathbf{E}_{2n} - \frac{\epsilon_1}{\epsilon_2} \mathbf{E}_{1n} \right) \mathbf{E}_t \mathbf{t} \right). \quad (11)$$

The stress balance on the interface can be rewritten as

$$[\mathcal{T} \cdot \mathbf{n}]_2^1 = [\boldsymbol{\sigma} \cdot \mathbf{n}]_2^1 - \Delta \mathbf{f}^e = -\gamma \kappa \mathbf{n}. \quad (12)$$

C. Nondimensionalization

The system are nondimensionalized by using the undisturbed core radius a for lengths, γ/μ_1 for velocities, γ/a for the pressure, $\mu_1 a/\gamma$ for time, V_0 for the voltage potential, and $\epsilon_2 \epsilon_0 V_0/a$ for surface charge density. The ratio of the physical property and dimensionless parameters are then denoted by

$$d = \frac{b}{a}, \quad \lambda = \frac{\mu_2}{\mu_1}, \quad Q = \frac{\epsilon_1}{\epsilon_2}, \quad E_b = \frac{\epsilon_0 \epsilon_2 V_0^2}{\gamma a}, \quad \Sigma = \frac{a \mu_1 \sigma_1}{\epsilon_0 \epsilon_2 \gamma}, \quad (13)$$

where E_b is an electric Weber number measuring the ratio of electrical to capillary pressures.²³

The Laplace equations are unchanged after nondimensionalization. The boundary conditions read as $\phi_2 = 0$ at $r = d$, and on the interface,

$$\phi_1^e = \phi_2^e, \quad (14a)$$

$$\mathbf{n} \cdot \mathbf{E}_2 - Q\mathbf{n} \cdot \mathbf{E}_1 = q, \quad (14b)$$

while the stress jump reads

$$\Delta \mathbf{f}^e = \frac{E_b}{2} \left([\mathbf{E}_{2n}^2 - Q\mathbf{E}_{1n}^2 - (1-Q)\mathbf{E}_t^2] \mathbf{n} + 2q\mathbf{E}_t \mathbf{t} \right), \quad (15)$$

together with the conservation law for q

$$q_t + \mathbf{u}_s \cdot \nabla_s q - q\mathbf{n} \cdot (\mathbf{n} \cdot \nabla) \mathbf{u}_s = \Sigma \mathbf{E}_{1n}, \quad (16)$$

where Σ is a dimensionless measurement of conductivity of core fluid. Equations for fluid motion are similar to the ones used in Ref. 23 and are not repeated here for brevity.

In the case of Stokes flow, capillary time scale is given by balancing surface tension and viscous force, $t_c \sim a\mu_1/\gamma$, while the electric relaxation time $t_e \sim \epsilon_0\epsilon_1/\sigma_1$. Therefore, the parameter $\Sigma = t_c/t_e$ measures the ratio of flow to charge relaxation time scales. Perfect conductor case is recovered if $\Sigma \rightarrow \infty$, which indicates that the relaxation occurs much faster than hydrodynamic deformation, hence the interface remains equipotential. On the other hand, in the limit $\Sigma \rightarrow 0$, surface charges are passively convected and stretched with deforming interface. In Sec. III, we will start to study the effect of moderate or low Σ on the system by linearizing the problem.

III. FORMULATION OF LINEARIZED PROBLEM

Linear dispersion relations pertaining to the stability of poorly conducting viscous liquid threads surrounded by a hydrodynamically passive region (air) and stressed by a radial electric field, have been derived by Ref. 15 when the surrounding electrode has a finite radius. Our study focuses on low Reynolds number flow and includes a viscous surrounding fluid with no base flows. Note that $\sigma_2 \neq 0$ would require a base flow in order to have a base steady state. Otherwise the linearized electrostatic problem (without base flow) would be decoupled from fluid problem. Furthermore, we define $V_0 = aq_0/\epsilon_0\epsilon_2$, where q_0 is the surface charge density at steady state. This gives electric Weber number as $E_b = q_0^2 a/\epsilon_0\epsilon_2\gamma$. We consider the stability of the quiescent perfectly cylindrical steady state (bars are used to denote base-flow quantities):

$$\bar{\mathbf{u}}_j = \mathbf{0}, \quad \bar{S} = 1, \quad \bar{\phi}_2 = \ln(d/r), \quad \bar{\phi}_1 = \ln(d), \quad \bar{q} = 1, \quad [\bar{p}] = 1 - \frac{E_b}{2}. \quad (17)$$

Perturbing about this state, linearizing the boundary conditions and assuming normal mode solutions proportional to $\exp(ikz + \omega t)$ allows for the problem to be cast into a rather simple eigenvalue system to determine $\omega(k)$, with instability present whenever $\text{Real}(\omega) > 0$. The perturbed interface position is described as

$$r = S(z, t) = 1 + \delta \hat{\eta} \exp(ikz + \omega t), \quad (18)$$

where δ is a small dimensionless number. Meanwhile, the flow is expressed in terms of a stream function so that $u_i = -(1/r)\partial\psi_i/\partial z$, $w_j = (1/r)\partial\psi_j/\partial r$ and writing $\psi_j(r, z, t) = \hat{\psi}_j(r) \exp(ikz + \omega t)$ provides the equation $E^4 \hat{\psi}_i = 0$, where the operator $E^2 = \frac{d^2}{dr^2} - \frac{1}{r} \frac{d}{dr} - k^2$. The solutions are

$$\hat{\psi}_j(r) = r \left(E_{1j} I_1(kr) + F_{1j} K_1(kr) + E_{2j} r I_0(kr) + F_{2j} r K_0(kr) \right), \quad (19)$$

where $E_{1j}, F_{1j}, E_{2j}, F_{2j}$ are unknown coefficients; regularity of solutions at the cylinder axis $r = 0$ implies $F_{11} = F_{21} = 0$. The solution for the linearized perturbation potential $\hat{\phi}_i(r) \exp(ikz + \omega t)$ proceeds along similar lines and satisfies zero order modified Bessel differential equation. Using boundary conditions and combining charge transport equation, the general solutions are readily

obtained,

$$\hat{\phi}_1 = A_1 I_0(kr), \quad \hat{\phi}_2 = A_2 (I_0(kr)K_0(kd) - K_0(kr)I_0(kd)), \quad (20)$$

where

$$A_1 = \frac{-\omega(kF + G)\hat{\eta} + ik(\hat{\psi}'_1 - \hat{\psi}_1)|_{r=1}G}{k(\omega(I_0F - QI_1G) - \Sigma I_1G)}, \quad (21)$$

$$A_2 = \frac{-[\omega(I_0 + QkI_1) + \Sigma kI_1\hat{\eta} + ik(\hat{\psi}'_1 - \hat{\psi}_1)|_{r=1}I_0]}{k(\omega(I_0F - QI_1G) - \Sigma I_1G)}, \quad (22)$$

with F and G defined as

$$F(k) = I_1(k)K_0(kd) + I_0(kd)K_1(k), \quad (23)$$

$$G(k) = I_0(k)K_0(kd) - I_0(kd)K_0(k). \quad (24)$$

The equations for fluid problem part are similar to those described in Ref. 23 and are summarized below. At tube wall we have no slip and no penetration condition,

$$\hat{\psi}_2(r = d) = 0, \quad \hat{\psi}'_2(r = d) = 0. \quad (25)$$

Continuity of velocities at fluid interface leads to

$$\hat{\psi}_1(r = 1) = \hat{\psi}_2(r = 1), \quad \hat{\psi}'_1(r = 1) = \hat{\psi}'_2(r = 1). \quad (26)$$

Then the modified tangential and normal stress balances are written as

$$(1 - \lambda)k^2\hat{\psi}_1 - \hat{\psi}'_1 + \lambda\hat{\psi}'_2 + \hat{\psi}''_1 - \lambda\hat{\psi}''_2 + E_b ik A_1 I_0(k) = 0, \quad (27)$$

$$\hat{p}_2 - \hat{p}_1 + ik(1 - \lambda)\hat{\psi}_1 - 2ik(\hat{\psi}'_1 - \lambda\hat{\psi}'_2) = (1 - k^2 - E_b)\hat{\eta} - \frac{E_b}{2}\hat{\phi}_{2r}^2, \quad (28)$$

where $\hat{\phi}_{2r}^2$ is solved at the beginning of this section. The above system is to be solved for six unknowns (E_{ij} and F_{ij}). After some computations we arrive at a linear and homogeneous system of six equations for the unknown vector $\mathbf{w} = [E_{11}, E_{21}, E_{12}, E_{22}, F_{12}, F_{22}]^T$ written in matrix form as

$$\mathbf{A}\mathbf{w} = 0. \quad (29)$$

The coefficient matrix is given in the Appendix A (derivations in a similar context in the absence of electric fields can be found in Ref. 30, for example). For a non-trivial solution of (29), we require $\det(\mathbf{A}) = 0$ and this provides the desired dispersion relation that can be solved to find the growth-rate $\omega(k)$.

A. Long wave behavior

The long-wave limit is explored first in the case of a single Stokes jet, $\lambda = 0$, by taking $k \rightarrow 0$. This yields the following asymptotic relations:

$$\omega \sim \frac{1}{6}\Lambda_1, \quad \text{for } \Lambda_1 > 0, \quad (30)$$

$$\omega \sim \frac{\Lambda_2}{2\Lambda_1}k^2, \quad \text{for } \Lambda_1 < 0, \quad \Lambda_2 < 0, \quad (31)$$

where $\Lambda_1 = 1 + E_b(3 - 4\ln d)$, $\Lambda_2 = \Sigma(E_b(\ln(d) - 1) - \ln(d))$. This switching mode is similar to the results reported in Ref. 15 for a single Navier-Stokes jet that is poorly conducting. Our result (31) can be obtained in their paper when Reynolds number tends to zero (square of inverse Ohnesorge number in their notation). Figure 2 shows evidence of this switching from results of full linear problem, where order one of growth rate that is independent of Σ is observed when $\Lambda_1 > 0$ in the left panel and a quadratic trend (this is shown in the inset of right panel for $\Sigma = 10$ in loglog

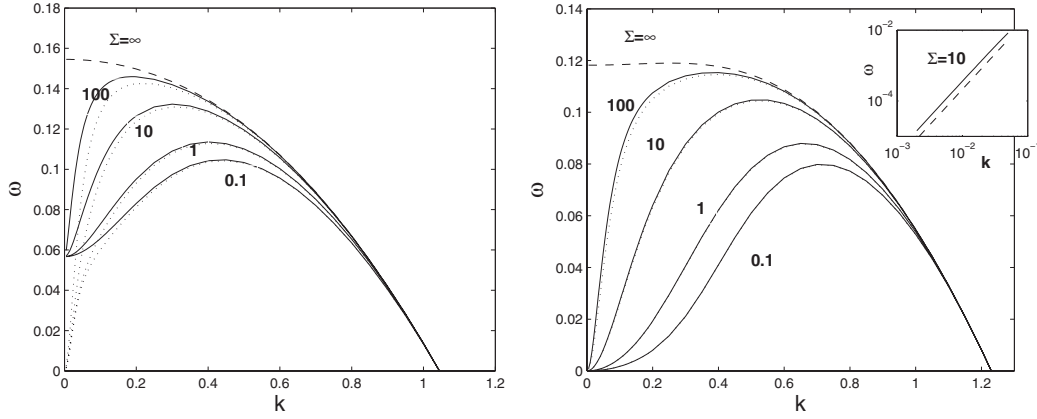


FIG. 2. The parametric dependence of the growth rates on Σ for $Q = 5$ and $d = 5$ fixed, in the Stokes limit $\lambda = 0$. $E_b = 0.192$ in left panel and $E_b = 0.768$ in right panel. The dotted lines show the corresponding results with the inclusion of annular viscous fluid, $\lambda = 0.001$ and the dashed line shows the limit of $\Sigma = \infty$ for $\lambda = 0$, namely the perfect conductor case.

plot where dashed line is long wave result) when $\Lambda_1, \Lambda_2 < 0$ for long waves in the right panel. Furthermore, (30) and (31) imply the possibility to stabilize long waves. For example, provided $E_b > 1$, the long waves are stabilized when

$$\ln d > \frac{1}{4} \left(3 + \frac{1}{E_b} \right). \quad (32)$$

Finally, it is interesting to notice that in (30), whenever $d < e^{3/4} \approx 2.117$, the electric field is always destabilizing. The value is different from the one obtained in perfect conductor limit for absolute destabilizing, which is $e \approx 2.718$. The permittivity ratio Q may enter to influence at higher order terms.

For two fluid system, $\lambda > 0$, however, the dominant mode follows a quadratic trend even though Λ_1 changes its sign as we found for $\lambda = 0$. The growth rate, as $k \rightarrow 0$, is determined by the following equation:

$$a_0 \omega^2 + b_0 \omega + c_0 = 0, \quad (33)$$

where

$$a_0 = 4\lambda + 6k^2 f(d), \quad (34)$$

$$b_0 = \frac{a_0}{2} \Sigma \ln(d) k^2 - f(d) (1 + E_b (3 - 4 \ln(d))) k^2, \quad (35)$$

$$c_0 = -\frac{\Sigma f(d)}{2} (\ln(d) + E_b (1 - \ln(d))) k^4, \quad (36)$$

with $f(d) = \ln(d) - (d^2 - 1)/(d^2 + 1)$. The details of linear stability are investigated next.

B. The effect of electric fields on linear stability

In this section, we investigate the influence of electric fields on the thread stability by numerically solving the linearized problem. Left panel of Fig. 2 depicts the effect of Σ on the linear dispersion relation in limit of a single Stokes jet, i.e., $\lambda = 0$, for $Q = 5$, $E_b = 0.192$ and $d = 5$. These parameters give positive value Λ_1 in (30) and order one growth rate is observed at long waves as discussed in Sec. III A. Clearly a decrease in Σ results in a decrease of growth rate for unstable modes. In addition, it is evident that the most dangerous mode is now located at intermediate wave numbers compared with the case of a perfect conductor²⁰ in dashed line, where $k = 0$ is the most unstable mode. In the right panel of Fig. 2, a larger E_b (such that $\Lambda_1 < 0$) leads to switching of dominant

mode for long waves which now follow a quadratic trend. Similarly, growth rate becomes smaller as Σ gets smaller. For the parameters that yield a quadratic growth in long waves, those curves become almost identical to those ones with a viscous external fluid included ($\lambda = 0.001$ in dotted lines). Inspection of both panels also reveals that when $\Sigma = 100$, namely, the conductivity of liquid thread is large, the linear growth rate for $k > 0.4$ is almost the same as the perfect conductor one as expected. But the sensitivity is captured in the long wave length range where the difference is obvious. Similarly, for fixed finite Σ , reduced relative electric permittivity Q results in a decreasing growth rate (not shown) as showed in Ref. 15 for a single jet.

Next we turn to the general case of two viscous fluids, i.e., $\lambda > 0$. The effect of various parameters is explored in Fig. 3 for $E_b = 0.25$, $Q = 10$, $\Sigma = 10$, $d = 5$, and $\lambda = 0.25$ unless otherwise indicated in figure. Each of panel (a)–(e) depicts growth rate curves when one of these parameters varies with the rest fixed. Similar to the perfect conductor limit, increasing the strength of electric fields extends the range of unstable modes. Short waves become unstable while the long waves are stabilized, provided that the dimensionless tube radius d is sufficiently far away from thread interface initially. In panel (a) with $d = 5$ fixed, a stable region for small k at $E_b = 4.5$ emerges, while a wide range of unstable short waves are obtained simultaneously. Increasing permittivity ratio Q seems not affecting growth rate significantly for the unstable modes as seen in panel (b). As a result, both maximum growth rate and cut off wavelength remain almost the same when Q varies. While the details of stable modes might be different which is beyond the scope of current study. As mentioned for $\lambda = 0$, increasing Σ increases growth rate; this also applies for $\lambda = 0.25$ in panel (c). That is likely saying that surface charge convection creates additional tangential flow that stabilizes thread. However, as λ increases further, large viscous drag from outer fluid reduces this effect and little changes in growth rate (not shown). The influence of external viscous fluid is studied in panel (d) by varying the viscosity ratio λ , where it is seen that growth rate reduces to a small level as λ becomes sufficiently large. As a result, annular region is effectively rigid compared to core fluid region, which hinders the development of perturbation. Tube radius d can also alter stability when the electrification level is fixed. Reducing tube radius d results more intense fields in the annular region. On the other hand, flow velocity scale becomes small as in the uncharged case.³¹ Panel (e) shows that overall growth rates become small as d decreases as expected. Meanwhile the range of unstable modes is extended, which is similar to the findings for perfect conductor in Ref. 23. In panel (f) the long wave result (33) is plotted together with the full curve for different electrode locations, which show agreement in the portion of small wavenumbers as expected.

Our results are in agreement with those discussed in Ref. 15 when the annular viscous effect is small. However, linear problem shows that growth rate is insensitive to Q and Σ when the two fluids have comparable viscosity. We show later by direct simulations that the breakup of liquid thread, however, is affected significantly in the nonlinear regime.

IV. BOUNDARY INTEGRAL METHOD

The boundary integral method is employed to solve the problem of a viscous thread immersed in another viscous fluid (see Refs. 31 and 23 for related studies). For the rest of our study, we only consider the simple case when the two fluids have the same viscosity ($\lambda = 1$), where the interfacial velocity is determined solely by the single layer potential as seen in (37)

$$u_\alpha(\mathbf{x}_0) = -\frac{1}{8\pi} \int_I M_{\alpha\beta}(\mathbf{x}, \mathbf{x}_0) \Delta f_\beta(\mathbf{x}) dl(\mathbf{x}), \quad (37)$$

where

$$\Delta f = \kappa \mathbf{n} - \frac{E_b}{2} ([\phi_{2n}^2 - Q\phi_{1n}^2 - (1-Q)\phi_{1t}^2] \mathbf{n} - 2q\phi_{1t} \mathbf{t}), \quad (38)$$

with $l(\mathbf{x})$ the arc length, κ the curvature of interface, q the surface charge density, and $\mathbf{n}(\mathbf{t})$ the unit normal (tangential) vector. The expression for the stress jump across fluid interface can be found in Ref. 17 which reviews mathematical formulations for leaky dielectric fluids. $M_{\alpha\beta}$ in (37) is the axisymmetric periodic Stokeslets which vanishes at tube wall, $r = d$,³¹ so that no slip boundary

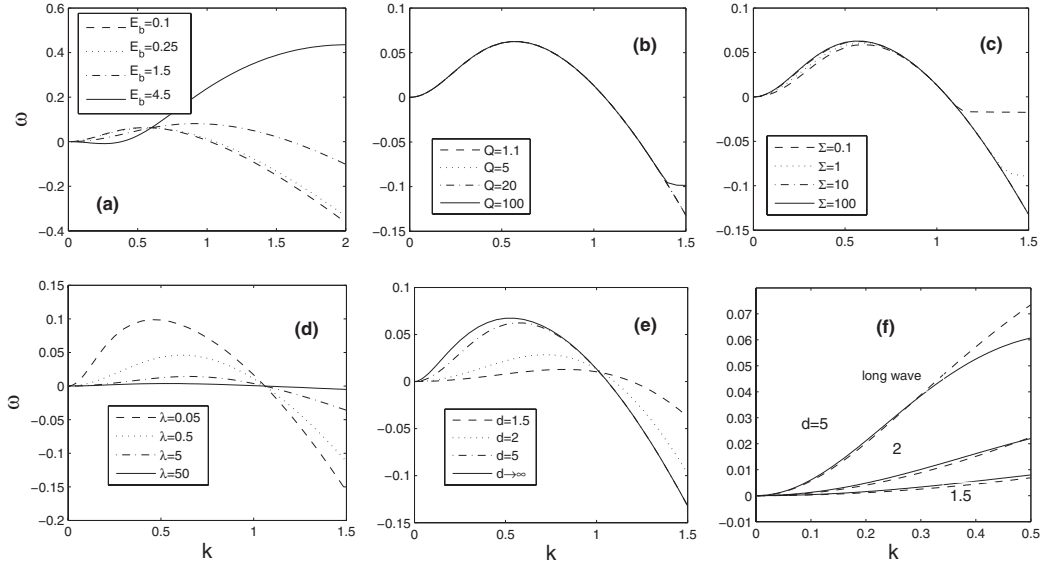


FIG. 3. Dispersion curves as a function of parameters $E_b = 0.25$, $Q = 10$, $\Sigma = 10$, $d = 5$, and $\lambda = 0.25$ except when indicated in figure. Panel (f) shows agreement of long wave results (33) on the results of full linear problem for different d .

condition is satisfied. The electrostatic potentials at thread surface, ϕ_1 and ϕ_2 when \mathbf{x}_0 is approached from region 1 and 2, respectively, are determined by

$$\frac{1}{2}\phi_1(\mathbf{x}_0) + \int_I \phi_1(\mathbf{x})P_n(\mathbf{x}, \mathbf{x}_0)r(\mathbf{x})dl = \int_I \phi_{1n}(\mathbf{x})P(\mathbf{x}, \mathbf{x}_0)r(\mathbf{x})dl, \quad (39)$$

$$-\frac{1}{2}\phi_2(\mathbf{x}_0) + \int_I \phi_2(\mathbf{x})P_n(\mathbf{x}, \mathbf{x}_0)r(\mathbf{x})dl = \int_I \phi_{2n}(\mathbf{x})P(\mathbf{x}, \mathbf{x}_0)r(\mathbf{x})dl, \quad (40)$$

where P is the axisymmetric periodic Green's function that vanishes at tube wall. In addition, due to the assumption that solutions are L -periodic, we impose no flux conditions at $z = 0$ and $z = L$, i.e., $\phi_{in}(z = 0, r) = \phi_{in}(z = L, r) = 0$. Hence, axial images are chosen so that $P_n(z = 0, r) = P_n(z = L, r) = 0$ is satisfied (also see the formulation in Ref. 23). By subtracting (40) from Q times (39) and using $\phi_1 = \phi_2$ at interface, an equation for surface potential is obtained,

$$\frac{1+Q}{2}\phi_1(\mathbf{x}_0) + (Q-1) \int_I \phi_1(\mathbf{x})P_n(\mathbf{x}, \mathbf{x}_0)r(\mathbf{x})dl = \int_I q(\mathbf{x})P(\mathbf{x}, \mathbf{x}_0)r(\mathbf{x})dl. \quad (41)$$

Directly subtracting (39) from (40) then leads to an equation for ϕ_{1n} ,

$$\phi_1(\mathbf{x}_0) = \int_I ((1-Q)\phi_{1n}(\mathbf{x}) + q) P(\mathbf{x}, \mathbf{x}_0)r(\mathbf{x})dl, \quad (42)$$

where q is solved from Eq. (16). The weak singularities in the kernels of the single-layer potential terms can be handled by Gauss-log quadratures and the regular integrals computed by standard Gauss-Legendre quadratures. Given interface shape and surface charge density q instantaneously, ϕ_1 (surface potential = ϕ_2) and ϕ_{1n} are readily to be obtained from (41) and (42), hence ϕ_{2n} from (14b).

V. SIMULATIONS ON NONLINEAR EVOLUTION AND DISCUSSION

A. Solution procedure

In this section, we study the nonlinear dynamics of charged threads through direct numerical simulations with initial condition of the form $r(z, 0) = a(1 + \delta \cos(kz)) = aS(z, 0)$, $q(z, 0) = 1$, where a is the unperturbed core thread radius and ka is the dimensionless wavenumber of the perturbation.

Results for $a \neq 1$ can be rescaled to the ones with $a = 1$. We have chosen this form in order to make comparison with previous studies.^{31,32} The boundary conditions of electric potentials are mentioned in Secs. II and IV: $\phi_2(z, r = d) = 0$, $\phi_1(z, r = S) = \phi_2(z, r = S)$, $Q\phi_{1n}(z, r = S) - \phi_{2n}(z, r = S) = q$, and $\phi_{in}(z = 0, r, t) = \phi_{in}(z = L, r, t) = 0$. Similarly, we have periodic boundary conditions for surface charge density, $q_z(z = 0, t) = q_z(z = L, t) = 0$. Periodic Stokeslets $M_{\alpha\beta}(\mathbf{x}, \mathbf{x}_0)$ and Green's function $P(\mathbf{x}, \mathbf{x}_0)$ are computed as explained in Refs. 23, 32, and 33, where no slip and constant potential boundary conditions are satisfied (see also Sec. IV). For-aft symmetry is imposed additionally and solution of half period is plotted for various quantities. Given interfacial shape and charge density at current time step, electric potential as well as its derivatives is calculated through (41) and (42), which updates the instantaneous stress jump (38). Then fluid velocities at interface is evaluated directly by (37), where no inversion of matrix is necessary since there is no double layer potential term. To proceed to next time step, interface position (we typically trace the interface using 90–180 points in half period) is updated by using kinematic boundary condition with explicit Euler method^{23,34}

$$\frac{d\mathbf{x}}{dt} = (\mathbf{u} \cdot \mathbf{n}) \mathbf{n}. \quad (43)$$

Surface charge density q , solved in the same node points as those used in boundary integral method, is then updated in Eq. (16) using finite difference method, where q is assumed to vary quadratically between collocation points.^{34,35} An implicit Euler scheme is used to advance q in time. This gain more stability than explicit method when Σ small.

The boundary integral code is tested against full linear theory and has been previously used to study the nonlinear evolution of a perfectly conducting thread inside a cylindrical tube in Ref. 23. In particular, evidence is provided in the upper panel of Fig. 4, where computed growth rates (in symbols) are compared with the results from linear theory (lines) for different wavenumbers. As showed in Sec. III, the growth rate differs little for different Σ when the two fluids are comparably viscous. Our numerical results for $\lambda = 1$ show good agreement on this by imposing the results on

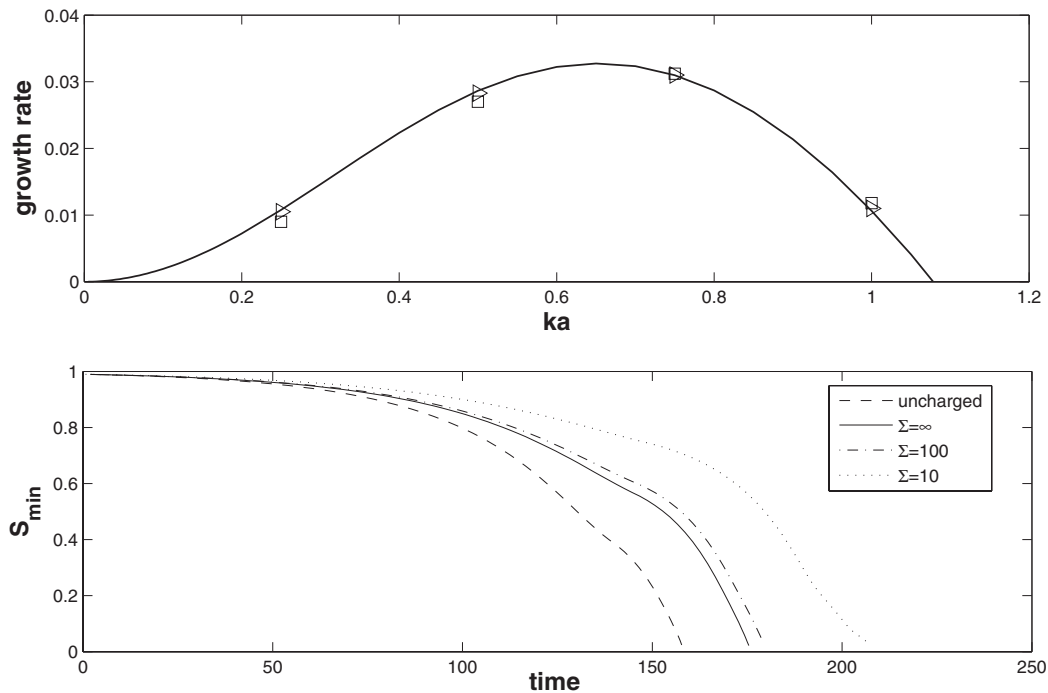


FIG. 4. (Upper panel) Linear growth rate test between numerical simulation and linear theory (solid curve) for $E_b = 0.32$, $Q = 5$. Triangle for $\Sigma = 100$, square for $\Sigma = 10$. (Lower panel) Time evolutions of minimum neck of liquid threads for different conductivities as indicated in figure for $ka = 0.5$ and $\delta = 0.01$. The most left curve is the uncharged case and solid line is the case of perfectly conducting core.

the same plot in Fig. 4, where triangle symbol stands for results with $\Sigma = 100$ and square is for $\Sigma = 10$. Still, when Σ is moderate, e.g., $\Sigma = 10$ in Fig. 4, growth rate appears slightly smaller than the linear theory when $ka < 0.6$, while slightly larger growth rate is obtained when $ka > 0.6$. This deviation occurs faster and more significantly when Σ is smaller, in which case, additional shear stresses produced by electric field quickly enter to play an important role. In addition, we start by perturbing interface shape with initial charge density fixed, which is slightly different from the setting in linearized problem (where we have perturbed q as well; agreement is better if we chose initial q in our simulation as in linearized problem) and may affect the results for moderate and small Σ , since then q will first slowly relax and adjust to the perturbed shape. The shear stresses may not follow the linear theory exactly even though the perturbation is small ($\delta = 0.01$ here). For simplicity, we chose $q(z, 0) = 1$. In the lower panel of Fig. 4, we compare the time evolutions of the minimum point of thread interface, S_{\min} by differing Σ . As indicated in figure, the dashed line is for a uncharged thread, the solid line is for a perfectly conducting thread, while the other two are of finite conductivity, $\Sigma = 100$ in dashed-dot line and $\Sigma = 10$ in dotted line respectively. Charged thread will breakup at a later time than the uncharged case, since electric force modifies normal stress and delay the thinning process as explained in Ref. 23. In order to make comparison with perfect conductor case from previous study, we notice that the relation of electric Weber number between Ref. 23 and current study is

$$E_b = \frac{E_b^*}{\ln^2 d}, \quad (44)$$

where E_b^* is the electric Weber number in Ref. 23. Inspection of Fig. 4 reveals that for $\Sigma > 0$, S_{\min} evolves at a similar pace at early stage for $t < 50$, after when the evolutions become different and further retardation of breakup is observed for small Σ . This is because convection of surface charge creates shear flow that opposes the fluid flow and more details are explained later. For the rest of current study, we consider the case when pinching does occur (either d is sufficiently large or E_b is sufficiently small physically). The discussion about the touchdown solution that is similar to those in Wang and Papageorgiou²³ will be carried out separately.

B. Pinching solution and satellite formation

The evolution of the surface position S , axial velocity w , and surface charge density q for a typical case with $Q = 5$, $\Sigma = 100$, $E_b = 0.32$, $ka = 0.5$, and $\delta = 0.1$, is shown in Fig. 5. Similar to the uncharged case, the modified capillary pressure (38) rises in the thinning region ($z/L = 0.5$), which pushes fluid toward the end of thread ($z/L = 0$). The evolutions of S and w to breakup are in panel (a) and (c), respectively, with the latter confirms the direction of the flow. In panel (b), evolution of the perturbation in solid line is compared against linear theory in dotted line, which shows good agreement even for $\delta = 0.1$ here. Nonlinear effect enters at dimensionless time $t \approx 40$, after when surface charge tends to accumulate on the shallow cone, which is seen in panel (d). In addition, the magnitude of q becomes relatively small in the necking region, which may lead to the guess that local pinching dynamics remains the same as in Ref. 23. This yet remains question at present and we show numerical investigation on local dynamics at the end of this section. In the last two panels of Fig. 5, the electrostatic contribution to the normal and tangential force is investigated, where we define

$$f_n^e = \frac{E_b}{2} (\phi_{2n}^2 - Q\phi_{1n}^2 - (1 - Q)\phi_{1t}^2), \quad f_t^e = -E_b q \phi_{1t}. \quad (45)$$

From panel (e) it is seen that similar to charge distribution, f_n^e is small in the necking region but large on the conical shallow cone region nearby (satellite drop region). Tangential electric force in panel (f) is seen to be only concentrated in the region $0.2 < z/L < 0.4$ and vanishingly small elsewhere, which implies the charge convection is only important as the necking region is forming in this case $\Sigma = 100$. But it still alters local flow field, hence to affect the thinning process and drop formation. As Σ decreases, charge convection is expected to play an important role in satellite drop formation, which is explored next by focusing on the electrical parameters Q , Σ , E_b . We begin the discussion

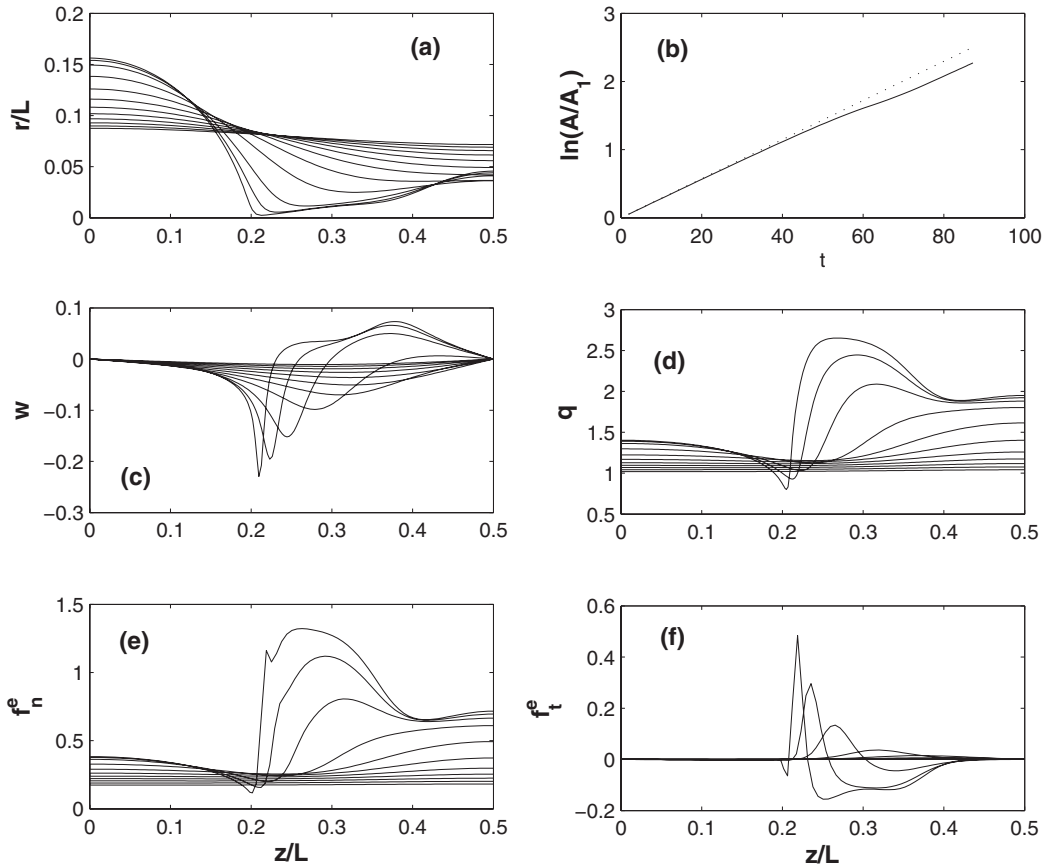


FIG. 5. Results on the evolution of thread profile, growth rate, axial velocity, and tangential electric force in half period. $E_b = 0.32$, $Q = 5$, $\Sigma = 100$, $ka = 0.5$, and $\delta = 0.1$. In panel (b), A_1 is the amplitude of initial perturbation and A is defined as half the difference of maximum and minimum of thread radius.

by showing Fig. 6, a “phase diagram” in (Σ, Q) space that illustrates the effect of Q , Σ on drop formation before pinching occurs, with the rest parameters fixed, $d = 5$, $E_b = 0.32$, and $\lambda = 1$. First of all, it is notable that the cases represented by the parameters in the last row ($\Sigma = 100$) show little difference on the satellite formation near breakup as expected as the permittivity ratio varies, because in these cases relatively large conductivity of core fluid forces surface charges to redistribute quickly, which is close to the perfect conductor case ($\Sigma = \infty$) in Ref. 23. In the panel of last row and last column, the interface shape of a uncharged thread is also plotted in dashed line, from where a larger satellite drop is observable when the thread is charged. As seen in perfect conductor case,²³ a local reduction in pressure is expected in the shallow cone region which leads to the formation of a larger satellite drop compared to the uncharged case, since more fluids are allowed to enter the satellite structure. Similar results are obtained here for $\Sigma = 100$ where tangential electric force is relatively small along most portion of surface.

As Σ decreases, results become subtle. The case of $\Sigma = 10$ is explored in the third row of Fig. 6, where no significant change is seen in the satellite formation. However, close inspection of them reveals that another thin neck tends to be formed between the thin thread and the small drop, at $z/L \approx 0.41$ for $Q = 10$. More satellite drops are likely to form after first pinchoff for large Q . We further investigate this by showing the evolution of S_{\min} and the profiles of normal and tangential part of electrostatic force close to breakup in Fig. 7. The panel (a) of Fig. 7 shows the evolution of S_{\min} which implies the thinning process is retarded further when $\Sigma = 10$ is fixed for large Q . This effect is not obvious when $\Sigma = 100$, which may be due to the difference on the polarization force. Satellite formation is shown in panel (b) for various Q , from where it is seen that pinching point is shifted further to left of $z/L = 0.2$ for relatively large Q . This is because near breakup, larger normal electric

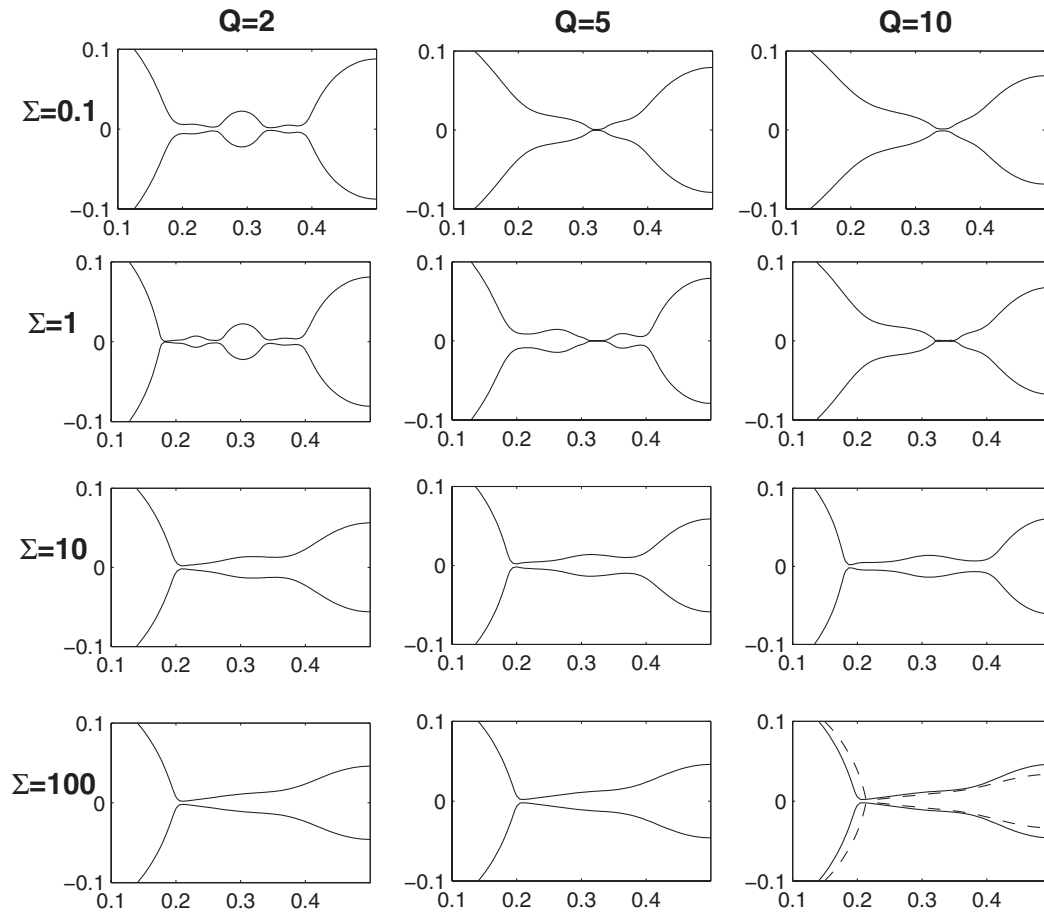


FIG. 6. Satellite drop formation near breakup for various parameters Q and Σ as indicated in the figure. Additional parameters $E_b = 0.32$, $d = 5$, and $ka = 0.5$. Dashed line in the last panel is the result of uncharged thread subject to the same initial interfacial perturbation.

force f_n^e is observed (see panel (c)) for larger Q , which reduces local pressure further to allow more fluid in satellite structure and retard thinning process. Notice that f_n^e does not show a clear minimum which is quite different from that in panel (e) in Fig. 5 where $\Sigma = 100$. Instead it tends to be large in the satellite region rather quickly. In addition, the dotted curve ($Q = 10$) clearly shows two peaks in normal force which corresponds to two thinning neck as we see in the panel in second row and third column. A second peak also tends to form in the $Q = 5$ case, whereas there is only one peak for $Q = 2$. The tangential electric force is included in panel (d) near pinching. The magnitude of tangential force is seen to be smaller for larger Q , where the dotted line show a positive peak around $z/L \approx 0.2$ and a negative peak around $z/L \approx 0.4$ as breakup is approached. This corresponds to our case $\Sigma = 10$, $Q = 10$ and is consistent with result observed in panel (c). As a result, the tangential electrostatic force provides pulling forces in opposite directions at $z/L \approx 0.2$ and $z/L \approx 0.4$, which supplies as additional forces to drive the pinching and is responsible for potential breakup around $z/L \approx 0.4$ after the first breakup, hence multiple satellite drop formation, which unfortunately cannot be traced by using current simulations. For fixed $\Sigma = 10$, the trend to multiple satellite drop formation is obvious when we increase the electric Weber number E_b (not shown).

More complicated situation occurs when $\Sigma = 0.1, 1$ as seen in the first and second row of Fig. 6, respectively. The shape and number of satellite drops are highly dependent on the electrical parameters one chooses. In addition, the retardation of breakup is not monotonic as Q increases as seen in panel (a) of Fig. 8 when $\Sigma = 1$ fixed. (The case of $\Sigma = 0.1$ is not shown, which also gives non-monotonic breakup times.) The $\Sigma = 1$ and $Q = 10$ case show a larger decreasing in S_{\min} than other two cases at early stage, $40 < t < 80$, but with a slower decreasing rate after $t \approx 90$ compared

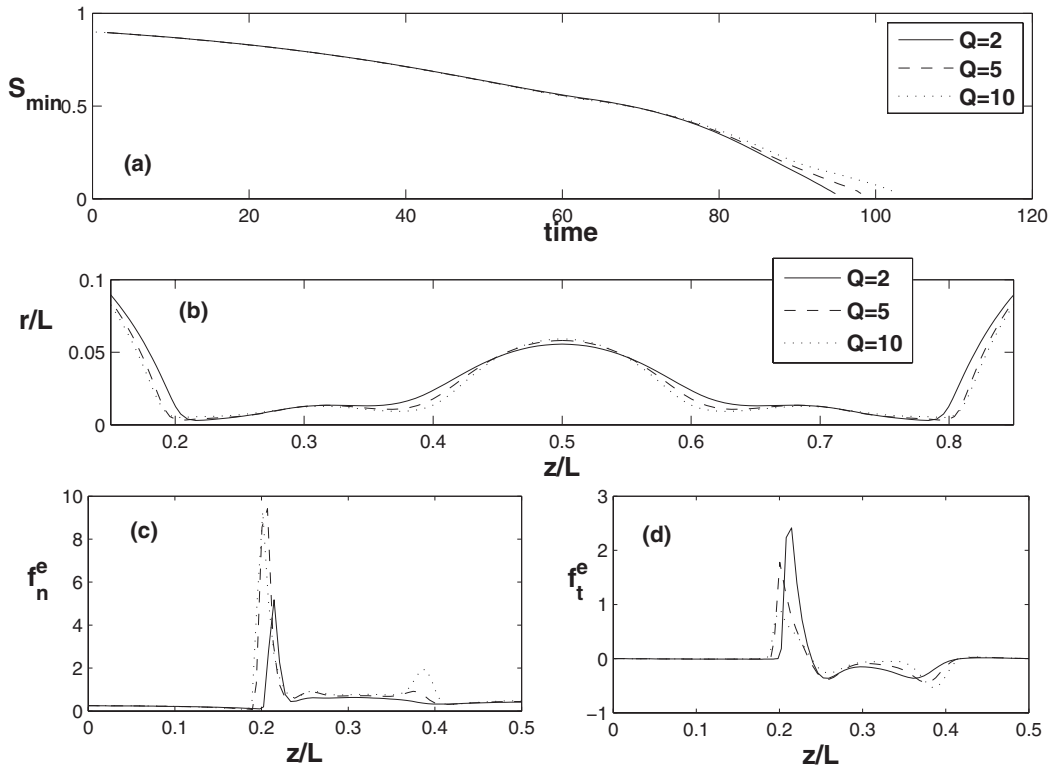


FIG. 7. The effect of Q on the minimal interfacial radius S_{\min} (a) and the satellite drop (b) as well as the electrostatic force f_n^e and f_t^e , (c) and (d), respectively, prior to breakup for $\Sigma = 10$.

with $Q = 2, 5$. But finally the case $Q = 5$ breaks up slower than the other two, at $t \approx 134.7$, in which case a bulge that connected to large or small drop can be observed (dashed line in panel (b) in Fig. 8). This bulge formation is also clear in the case of $Q = 10$, in which case one possible scenario involves pinching accompanied by the formation of satellites between the bulges and the retraction of bulges into the large drops afterwards. For the small satellite drops between the main drops, they are seen to tend to form more spherical shapes than a conical wedge in large conduction case. One explanation is that due to moderate and small conduction, surface charges relax slowly and tend to minimize the surface area locally to maintain a low energy level. The electrostatic force is also investigated as shown in panel (c) in Fig. 8, where at time close to breakup, one can see the complicated profiles of the normal component of electric force, which implies that multiple thin necks that possibly lead to multiple locations of breakup afterwards. The tangential electric force from panel (d) of Fig. 8 provides further evidence on the opposite directional stretching that is responsible for potential small drops formation after the first breakup.

In Fig. 9, we further compare the effect of electric tangential force due to moderate and low conduction on thread deformation at early stage. The surface shape $S(z, t)$, surface charge density $q(z, t)$, electric tangential force $f_t^e(z, t)$, and axial velocity $w(z, t)$ for $\Sigma = 1$ $Q = 5$ are shown in upper two panels at $t = 66.29$ and $t = 94.69$. The same physical quantities are plotted in lower panels for $\Sigma = 10$ when the thread has almost the same S_{\max}/S_{\min} as the previous one. When $\Sigma = 1$, we see that at $t = 66.29$ (panel (a)) surface charge density has a minimum in magnitude at $z/L \approx 0.25$ with larger q at smaller thread radius. When $\Sigma = 10$, thread evolves to a similar location at an earlier time, $t = 47.35$ and surface charge density has a similar spatial distribution but with a relatively flat profile for $z/L < 0.25$. At a later time, $t = 75.76$ for $\Sigma = 10$, q continues evolving with S and becomes much larger along region $z/L > 0.3$ in panel (d) than (b) at $t = 94.69$ for $\Sigma = 1$. Meanwhile, tangential force f_t^e is smaller when $\Sigma = 10$ in panel (c) and (d) compared to $\Sigma = 1$ in panel (a) and (b). It seems that when conduction is strong, charges tend to accumulate at regions with small thread radius quickly. Tangential electric force inhibits this trend when Σ small.

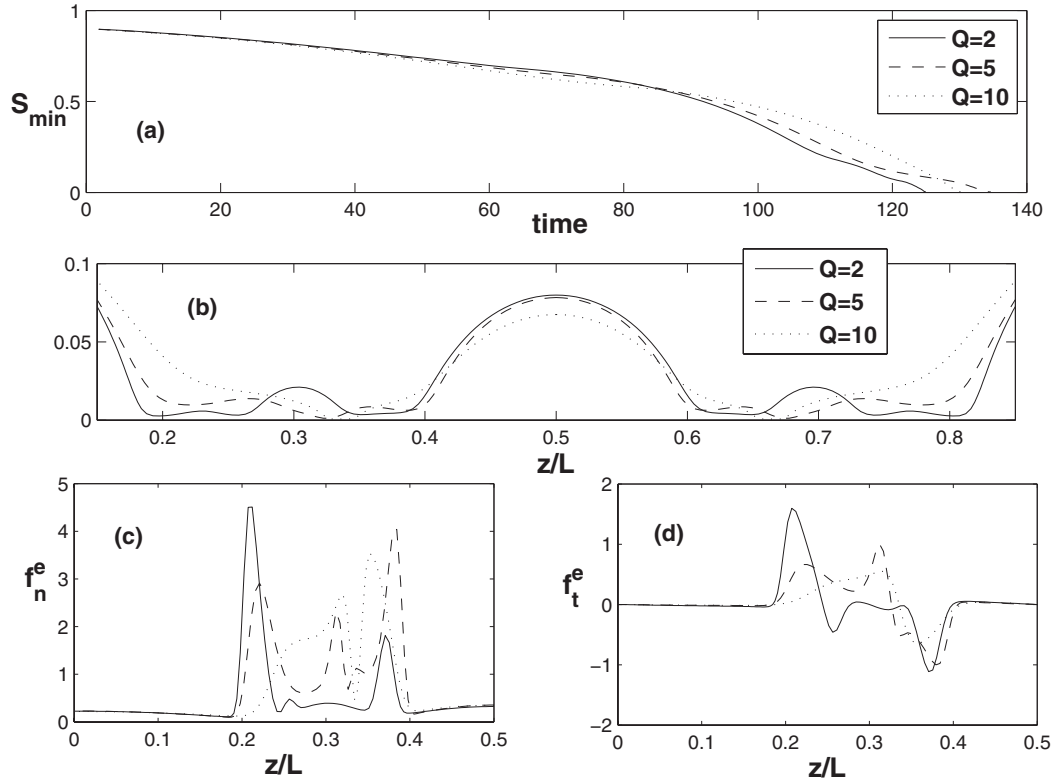


FIG. 8. The effect of Q on the minimal interfacial radius S_{\min} (a) and the satellite drop (b) as well as the electrostatic force f_n^e and f_t^e , (c) and (d), respectively, prior to breakup for $\Sigma = 1$.

As a result, the thread experiences more electric shearing forces when conduction is weak and the thread evolves more slowly (see the axial velocities in dotted lines). At later times, as seen in Fig. 6, more satellite drops are expected to form for weak conduction, where electric shearing force plays an important part. In the absence of electric field, the role of interfacial shear is already attributed to the multiple small satellite formation.³⁶ We argue that the electric shear stress serves in a similar manner to promote the multiple drop formation.

C. Scaling analysis and long wave approximation

Without electric field, the scalings for the balance on pinching is introduced in Ref. 7. A simple balance of viscous drag and capillary force gives $S \sim z \sim \tau$, while axial velocity increases slowly as $w \sim \ln(\tau)$ where τ is the remaining time to breakup. The balance remains the same when the perfect conductor limit is considered in Ref. 23 (confirmed numerically) where only normal stress balance is modified by electric field. When the conductivity of the core thread is finite, the scalings may be altered. We consider the ratio of electric force and capillary force at the minimum point of thread interface, $f_n^e/f_c = E_b/2 (\phi_{2n}^2 - Q\phi_{1n}^2 - (1-Q)\phi_t^2)/\kappa$. Figure 10 shows f_n^e/f_c for various Σ and Q as indicated in figure with $E_b = 2$ and $d = 5$ fixed. All data show the trend toward a finite value instead of a vanishingly small one, which indicates the local dynamics may be changed in these cases (see Ref. 21 for similar argument for an electrified jet with different viscosities). In fact, our results show that for relatively large Σ , convergence to the Lister-Stone scalings⁷ is observed, though at a much later time (closer to singularity) compared to the results in Ref. 23, because now double cone structure is only formed locally. For relatively small Σ , the axial velocity still shows $w \sim \ln(\tau)$ but the coefficient is quite different, which implies different angles at breakup. No existing theory can explain this universally to our best knowledge so far, or whether a universal theory exists is unclear.

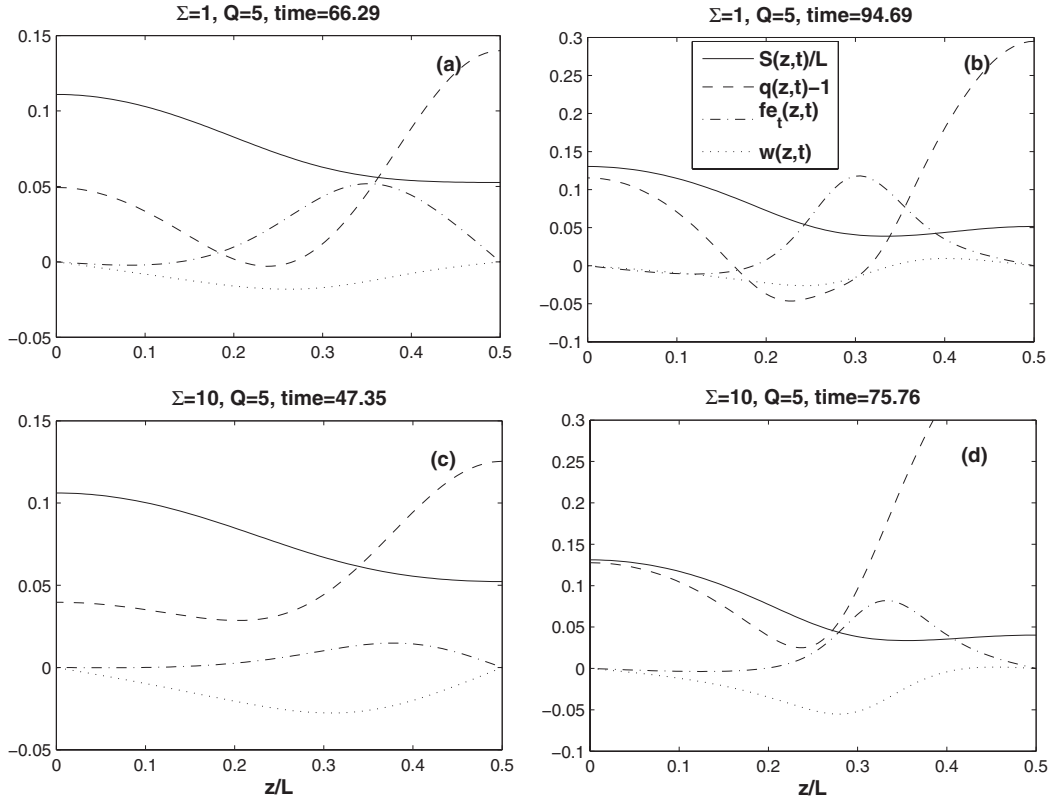


FIG. 9. Physical quantities of surface position $S(z, t)$, surface charge density $q(z, t) - 1$, tangential electric force $f_t^e(z, t)$ and axial velocity $w(z, t)$.

We also investigate the two phase flow breakup by deriving a long wave model (B10)–(B12) under the assumption that the whole pipe is slender and core fluid is much viscous than the annular one, $\lambda = \delta^2 \lambda_0$ with δ the slenderness parameter, so that we retain the viscous effect of annular region. The Stokes version is given as following (the details of derivation can be found in Appendix B):

$$S_t + \frac{1}{2} S w_z + w S_z = 0, \quad (46)$$

$$-3 \frac{(S^2 w_z)_z}{S^2} + \left(\frac{1}{S} - \delta^2 S_{zz} - \frac{E_b}{2} q^2 \right)_z + 2\lambda_0 G(S, d) \frac{w}{S^2} - 2E_b \frac{q}{S} \phi_{1z} = 0, \quad (47)$$

$$q_t + \frac{1}{2} q w_z + w q_z = -\delta^2 \Sigma (\phi_{1r}^1 - S_z \phi_{1z}), \quad (48)$$

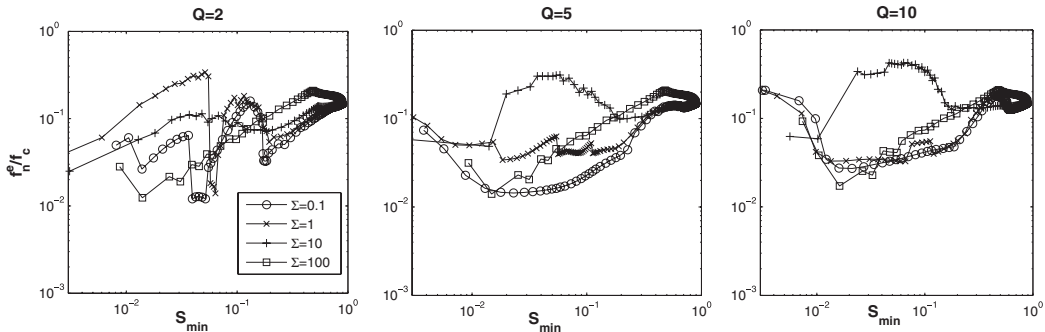


FIG. 10. Balance of normal electrostatic force and capillary force as the breakup is approached for various Q and Σ .

where $2\lambda_0 G(S, d)w/S^2$ in (47) is the contribution of annular viscous drag, $E_b/2q^2$ is the radial repulsion of surface charge and $E_b q/S\phi_{1z}$ is contribution from electric tangential force. Polarization force due to permittivity gradient does not enter the leading order. Charge diffusion in (48) is also neglected. We further notice that dimensionless conductivity Σ stays at higher order provided $\Sigma < \delta^{-2}$, which is suitable for current case when considering poor conductor. This term is not included in our calculations. Numerical simulation of (46)–(48) is carried out by using an efficient PDE solver EPDCOL,³⁷ which has been used to simulate slender jet problem successfully in Refs. 29 and 38. The method used finite element collocation in space and Gear's method in time. We typically take 4000 points over one period of domain. The accuracy is assured by comparing the numerical results with the linear growth rate (not shown) when small perturbations are introduced in S and q initially. For the results reported here, we take initial conditions as

$$S(z, t = 0) = 1 + 0.1 \cos(2\pi z/L), \quad q(z, t = 0) = 1, \quad w(z, t = 0) = 0. \quad (49)$$

The boundary conditions are

$$S_z(0, t) = S_{zzz}(0, t) = 0, \quad S_z(L, t) = S_{zzz}(L, t) = 0, \quad (50)$$

$$w(0, t) = w(L, t) = 0, \quad (51)$$

$$q_z(0, t) = 0, \quad q_z(L, t) = 0. \quad (52)$$

The tube radius is fixed as $d = 5$ and $\lambda_0 = 1$. Following Ref. 3, $\delta^2 S_{zz}$ is retained with $\delta = 0.01$. Simulation with other δ (e.g., $\delta = 0.1$) gives visually the same growth rate and interfacial shapes for the d used here. Numerical results are shown in Fig. 11, where panel (a) show the interface shape together with satellite formation near pinchoff ($S_{\min} < 0.001$). It is seen that as E_b increases, the satellite structure tends to get small. This is qualitatively in agreement with our full simulation, in

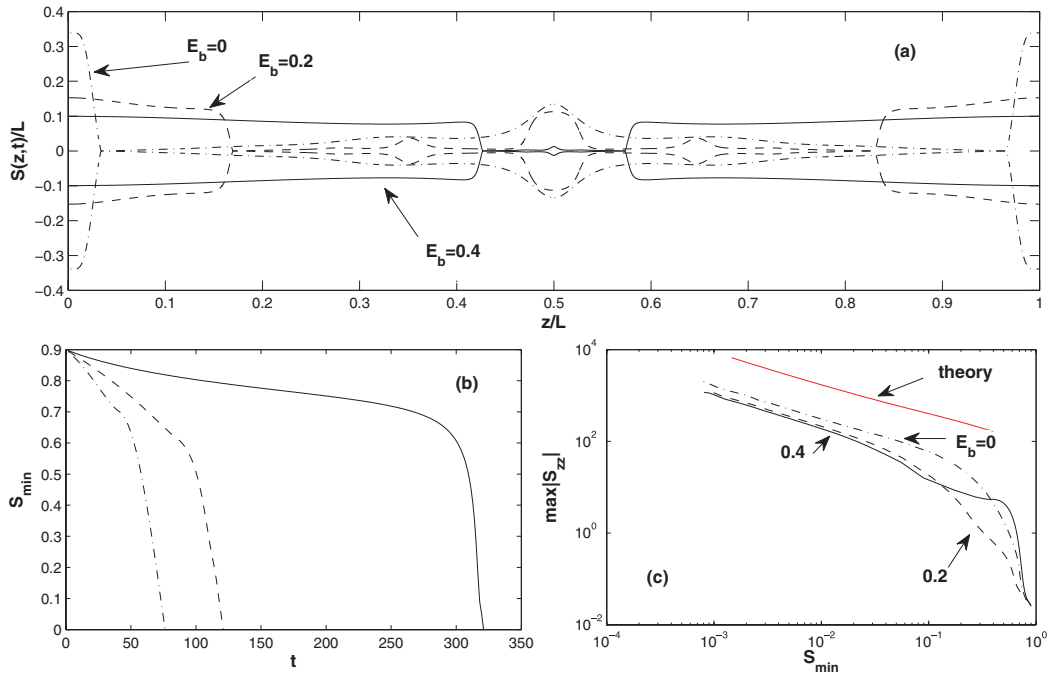


FIG. 11. The effect of E_b on the surface shape and satellite drop formations is shown in panel (a). Panel (b) shows the evolution of minimum thread radius for different E_b showing the retardation of breakup for charged threads. Panel (c) shows nonlinear simulations agree with the scalings near breakup. The imposed solid line on top indicates the evolution of $1/Sw^2$, which grows in parallel with $\max|S_z|$ as expected from (55).

the two panels in first column in Fig. 6, where small drop structures do appear when Σ becomes small. On the other hand, this is quite different from the case when conduction is large, where larger satellite drop is expected at larger E_b .²³ The retardation of electric field is shown in panel (b) which agrees with our previous results from full axisymmetric simulation. Now with this reduced model, we can carry out the simulation close to breakup point to investigate the possible scalings, which is summarized in panel (c) in Fig. 11 and will be discussed after we derive the scalings. In computation, adaptive grid is used when the minimum thread radius is small. In particular we set the local grid size inversely proportional to the maximum of S_{zz} . It turns out that the long wave model in fact leads to new scalings even in the uncharged problem compared to the ones in Ref. 7. By simple balance in (47), we find

$$w_{zz} \sim (S^{-1})_z \sim G(S, d) \frac{w}{S^2}, \quad (53)$$

which, together with $w \sim z/\tau$, leads to

$$S(z, t) \sim \tau, \quad z \sim \tau (\ln(1/\tau))^{1/2}, \quad w \sim (\ln(1/\tau))^{1/2}, \quad (54)$$

hence

$$S_{zz} \sim \frac{1}{\tau \ln(1/\tau)} \sim \frac{1}{S w^2}. \quad (55)$$

Indeed the inertia is negligible in this case since $w_t \sim \tau^{-1} (\ln(1/\tau))^{1/2}$, which is asymptotically much smaller than other terms in axial momentum equation. The electric force is also not contributing on the pinchoff by using (54). As a result, axial length scale is different from $\lambda = 1$ (uncharged and perfect conductor) case with square root of a logarithmic term, which indicates a weak dependence on initial condition and slow convergence to final scalings.³⁹ In panel (c) of Fig. 11, nonlinear computations for various E_b confirm our prediction (55), where the maximum S_{zz} grows as $S \rightarrow 0$ and the imposed solid line above is the evolution of $1/S w^2$. Whether the scalings can be identified from full axisymmetric simulations or not (λ should be extended to larger range as well) is a future task, which requires a highly adaptive grid due to the complex structure of satellites. Finally, we note that even though the scalings are confirmed by simulation, the local shapes of S and w do not collapse to single curves. Thus self-similarity solutions may not exist. In fact, if we set $S = \tau H$, $w = \ln(1/\tau)^{1/2} V$ with $z = \tau \ln(1/\tau)^{1/2} \xi$, at leading order we formally get a set of ODE for H and V which are the same as the ones derived in Ref. 7, where they argued nonexistence of self-similarity solutions. The boundary conditions for H, V are different from theirs though,

$$H \sim \xi (\ln \xi)^{1/2}, \quad V \sim (\ln \xi)^{-1/2}, \quad \text{as } \xi \rightarrow \pm\infty. \quad (56)$$

Details of study of this lies beyond the scope of current study and hence are also left as future investigations.

VI. CONCLUSIONS

We have investigated the stability of an axisymmetric charged viscous thread immersed in another viscous fluid confined to a cylindrical tube through a leaky-dielectric model. Linear stability analysis has been carried out, which show weak dependence of growth rate on electric parameters Q and Σ when the two fluids are comparably viscous. However, direct numerical simulation based on boundary integral method shows that the drop formation and rupture time are affected significantly for moderate or low Σ/Q in nonlinear regime, where electric tangential force plays an important role to provide additional shear stress to affect the nonlinear evolution. Based on the numerical results, multiple satellite drops tend to be formed when $\Sigma < 10$ for fixed electrification level. On the pinchoff, the local dynamics may be different from the perfect conductor case, for which an attempt to search explanation is made by deriving and simulating a long wave model. New scalings are predicted and confirmed by nonlinear simulations. But whether these scalings can be obtained from direct simulation on the full problem is still unclear.

ACKNOWLEDGMENTS

I would like to thank Professor Demetrios T. Papageorgiou of Imperial College London for some useful discussions. I also would like to thank Professor Michael Siegel and Professor Michael Booty of New Jersey Institute of Technology for their encouragement and support. This work is partly supported by National Science Foundation (NSF) Grant No. DMS-1009105.

APPENDIX A: MATRIX COMPONENTS FOR THE LINEAR PROBLEM

In this appendix, we document the elements of 6×6 matrix $A = (a_{ij})$, defined in Eq. (29) as following:

$$\begin{aligned}
 a_{11} &= I_1(k), & a_{12} &= I_0(k), & a_{13} &= -I_1(k), \\
 a_{14} &= -I_0(k), & a_{15} &= -K_1(k), & a_{16} &= -K_0(k), \\
 a_{21} &= kI_0(k), & a_{22} &= 2I_0(k) + kI_1(k), \\
 a_{23} &= -kI_0(k), & a_{24} &= -2I_0(k) - kI_1(k), \\
 a_{25} &= kK(k), & a_{26} &= -2K_0(k) + kK_1(k), \\
 a_{31} &= a_{32} = a_{41} = a_{42} = 0, \\
 a_{33} &= I_1(kd), & a_{34} &= dI_0(kd), \\
 a_{35} &= K_1(kd), & a_{36} &= dK_0(kd), \\
 a_{43} &= kI_0(kd), & a_{44} &= 2I_0(kd) + kdI_1(kd), \\
 a_{45} &= -kK_0(kd), & a_{46} &= 2K_0(kd) - kdK_1(kd), \\
 a_{51} &= 2kI_1(k) - E_b I_0(k) \frac{kI_1(k)F + kI_0(k)G}{\omega(I_0(k)F - QI_1(k)G) - \Sigma I_1(k)G}, \\
 a_{52} &= 2(I_1(k) + kI_0(k)) - E_b I_0(k) \frac{kI_0(k)F + (kI_1(k) + 2I_0(k))G}{\omega(I_0(k)F - QI_1(k)G) - \Sigma I_1(k)G}, \\
 a_{53} &= -2\lambda k I_1(k), & a_{54} &= -2\lambda(I_1(k) + kI_0(k)), \\
 a_{55} &= -2\lambda k K_1(k), & a_{56} &= -2\lambda(kK_0(k) - K_1(k)), \\
 a_{61} &= 2k(kI_0(k) - I_1(k)) - \frac{kI_1(k)}{\omega} \left(1 - k^2 - E_b \left(1 - \frac{F}{I_1(k)} \frac{(kI_0^2(k) + QkI_1^2(k))\omega + \Sigma kI_1^2(k)}{\omega(I_0(k)F - QI_1(k)G) - \Sigma I_1(k)G} \right) \right), \\
 a_{62} &= 2kI_1(k)k - \frac{kI_0(k)}{\omega} \left(1 - k^2 - E_b \left(1 - F \frac{(2I_0(k) + kI_1(k) + QkI_1(k))\omega + \Sigma kI_1(k)}{\omega(I_0(k)F - QI_1(k)G) - \Sigma I_1(k)G} \right) \right), \\
 a_{63} &= -2\lambda k(kI_0(k) - I_1(k)), & a_{64} &= -2\lambda k^2 I_1(k), \\
 a_{65} &= 2\lambda k(kK_0(k) + K_1(k)), & a_{66} &= 2\lambda k K_1(k)k.
 \end{aligned}$$

The perfect conductor limit is recovered as $\Sigma \rightarrow \infty$ as expected. Then the contributions from tangential field in a_{51} and a_{52} vanish and the part inside bracket of last term in a_{61} and a_{62} reduces to

$$1 - k^2 - E_b \left(1 - k \frac{F}{G} \right), \quad (\text{A1})$$

which recovers the results in Ref. 23 by letting $E_b = E_b^*/\ln^2 d$, where E_b^* is the electric Weber number used in Ref. 23.

APPENDIX B: DERIVATION OF ONE DIMENSIONAL MODEL

In this section, we briefly document the asymptotic analysis that leads to the one dimensional equations. We assume the axial length scale is much larger than the radial one with slenderness parameter $\delta = a/l \ll 1$. Following Refs. 29 and 40, we introduce the expansion for electric potentials, $\phi_i \sim \phi_i^0 + \delta^2 \phi_i^1 + \dots$ with similar expressions for the other physical quantities.

The electric potentials satisfy the Laplace equation (1) and to leading order we have

$$\phi_{irr}^0 + \frac{1}{r} \phi_{ir}^0 = 0, \quad i = 1, 2. \quad (\text{B1})$$

Using boundary conditions (14) at $r = S^0(z, t)$, which in leading order of long wave limit are $\phi_1^0 = \phi_2^0$ and $Q\phi_{1r}^0 - \phi_{2r}^0 = q^0$, together with regularity condition $\phi_{1r}^0(r=0) > 0$ and $\phi_2^0(r=d) = 0$, yield the solutions for electric potentials

$$\phi_1^0 = -S^0 q^0 \ln(S^0/d), \quad \phi_2^0 = -S^0 q^0 \ln(r/d). \quad (\text{B2})$$

The equation for surface density on $r = S^0$ now becomes (by considering $R = 0$ first)

$$q_t^0 + w_1^0 q_z^0 + w_1^0 q_z^0 + \frac{q^0 u_1^0}{S^0} = -\delta^2 \Sigma (\phi_{1r}^1 + S_z^0 \phi_{1z}^0), \quad (\text{B3})$$

where Σ enters the leading order if $\Sigma \sim \delta^{-2}$ and ϕ_{1r}^1 is obtained by solving the equation in higher order $\phi_{1rr}^1 + \phi_{1r}^1/r + \phi_{1zz}^0 = 0$. From now on, we drop the superscript 0 but retain 1 to emphasize the high order term.

In the fluid region, we consider the Navier-Stokes equations. In order to take both core and annular fluids into account, we take the annular fluid to be less viscous, $\lambda = \delta^2 \lambda_0$. We further ignore the inertial effect in annular region, which amounts to assume $Re_2 < O(\delta^2)$. The axial momentum equation then gives

$$p_{2r} = 0, \quad p_{2z} = \frac{\lambda_0}{r} (r w_{2r}), \quad (\text{B4})$$

whose solutions are readily to be obtained, by using continuity equation

$$w_2 = \frac{1}{\lambda_0} \left(\frac{r^2}{4} p_{2z} + A \ln(r) + B \right), \quad (\text{B5})$$

$$u_2 = -\frac{1}{\lambda_0} \left(\frac{r^3}{16} p_{2zz} - \frac{r}{4} A_z + \frac{r \ln(r)}{2} A_z + \frac{r}{2} B_z \right) + \frac{C}{r}, \quad (\text{B6})$$

where A , B , and C are functions of z and t . In the core, $w_1 = w_1(z, t)$ in the leading order, which is independent of radial coordinate. Using continuity equation, $u_1 = -r w_{1z}/2$ as in the standard single fluid jet problem.^{3,40}

On the interface, the tangential and normal stress balances in leading order, read as

$$u_{1z} + w_{1r}^1 + 2S_z(u_{1r} - w_{1z}) - \lambda_0 w_{2r} = -E_b q \phi_{1z}, \quad (\text{B7})$$

$$p_1 - p_2 + w_{1z} = \frac{1}{S} - \delta^2 S_{zz} - \frac{E_b}{2} q^2, \quad (\text{B8})$$

where in normal stress balance, $\delta^2 S_{zz}$ is retained as in Ref. 3 and we notice that Q can only enter the system at next order $O(\delta^2)$. The higher order w_{1r}^1 is obtained from axial momentum equation,

$$w_{1r}^1 = \frac{r}{2} (\bar{R}e(w_{0r} + w_0 w_{0z}) - w_{0zz} + \kappa_z - E_b q q_z), \quad (\text{B9})$$

where $Re_1 = \delta^2 \bar{R}e$.

Therefore, with no-slip and no-penetration boundary conditions at wall, $w_2(r=d) = u_2(r=d) = 0$ and continuous velocity condition along $r = S$, $w_1 = w_2$ and $u_1 = u_2$, and the stress

balances above, after some algebra we arrive at the evolution equations for S , w , and q , namely, Eqs. (B10)–(B12):

$$S_t + \frac{1}{2}S w_z + w S_z = 0, \quad (\text{B10})$$

$$\bar{R}e (w_t + w w_z) = 3 \frac{(S^2 w_z)_z}{S^2} - \left(\frac{1}{S} - \delta^2 S_{zz} - \frac{E_b}{2} q^2 \right)_z - 2\lambda_0 G(S, d) \frac{w}{S^2} - 2E_b \frac{q}{S} \phi_{1z}, \quad (\text{B11})$$

$$q_t + \frac{1}{2}q w_z + w q_z = -\delta^2 \Sigma (\phi_{1r}^1 - S_z \phi_{1z}), \quad (\text{B12})$$

where $\phi_{1r}^1 = r/2 (Sq \ln(S/d))_{zz}$, $\phi_{1z} = -(Sq \ln(S/d))_z$ and

$$G(S, d) = \frac{S^2 + d^2}{S^2 - d^2 - (S^2 + d^2) \ln(S/d)}. \quad (\text{B13})$$

Notice that in the uncharged flow case with $\bar{R}e = 0$, considering $d \rightarrow \infty$ and rescaling $\lambda_0 = \ln(d)\lambda_1$, or $\lambda = \delta^2 \ln(d)\lambda_1$, we obtain formally the equation in Ref. 7,

$$S_t + \frac{1}{2}S w_z + w S_z = 0, \quad (\text{B14})$$

$$2\lambda_1 w - 3(S^2 w_z)_z + S^2 \left(\frac{1}{S} - \delta^2 S_{zz} \right) = 0. \quad (\text{B15})$$

- ¹L. Rayleigh, "On the instability of a cylinder of viscous liquid under the capillary force," *Philos. Mag.* **34**, 145–154 (1892).
- ²S. Tomotika, "On the instability of a cylindrical thread of a viscous liquid surrounded by another viscous fluid," *Proc. R. Soc. London, Ser. A* **150**, 322–337 (1935).
- ³J. Eggers and T. F. Dupont, "Drop formation in a one-dimensional approximation of the navier-stokes equations," *J. Fluid Mech.* **262**, 205–221 (1994).
- ⁴J. Eggers, "Universal pinching of 3D axisymmetric free-surface flow," *Phys. Rev. Lett.* **71**, 3458–3460 (1993).
- ⁵D. T. Papageorgiou, "On the breakup of viscous liquid threads," *Phys. Fluids* **7**, 1529–1544 (1995).
- ⁶R. F. Day, E. J. Hinch, and J. R. Lister, "Self-similar capillary pinchoff of an inviscid fluid," *Phys. Rev. Lett.* **80**, 704 (1998).
- ⁷J. R. Lister and H. A. Stone, "Capillary breakup of a viscous thread surrounded by another viscous fluid," *Phys. Fluids* **10**, 2758–2764 (1998).
- ⁸J. Eggers and E. Villermeaux, "Physics of liquid jets," *Rep. Prog. Phys.* **71**, 036601 (2008).
- ⁹D. A. Saville, "Electrohydrodynamic instability: Fluid cylinders in longitudinal electric fields," *Phys. Fluids* **13**, 2987–2994 (1970).
- ¹⁰A. J. Mestel, "Electrohydrodynamic stability of a highly viscous jet," *J. Fluid Mech.* **312**, 311–326 (1996).
- ¹¹D. A. Saville, "Stability of electrically charged viscous cylinders," *Phys. Fluids* **14**, 1095–1099 (1971).
- ¹²M. M. Hohman, M. Shin, G. Rutledge, and M. P. Brenner, "Electrospinning and electrically forced jets. I. Stability theory," *Phys. Fluids* **13**, 2201 (2001).
- ¹³A. L. Huebner and H. N. Chu, "Instability and breakup of charged liquid jets," *J. Fluid Mech.* **49**, 361–372 (1971).
- ¹⁴D. A. Saville, "Electrohydrodynamic instability: Effects of charge relaxation at the interface of a liquid jet," *J. Fluid Mech.* **48**, 815–827 (1971).
- ¹⁵J. M. López-Herrera, P. Riesco-Chueca, and A. M. Gañón-Calvo, "Linear stability analysis of axisymmetric perturbations in imperfectly conducting liquid jets," *Phys. Fluids* **17**, 034106 (2003).
- ¹⁶J. R. Melcher and G. I. Taylor, "Electrohydrodynamics: A review of the role of interfacial shear stresses," *Annu. Rev. Fluid Mech.* **1**, 111–146 (1969).
- ¹⁷D. A. Saville, "Electrohydrodynamics: The Taylor-Melcher leaky dielectric model," *Annu. Rev. Fluid Mech.* **29**, 27–64 (1997).
- ¹⁸F. Li, X. Yin, and X. Yin, "Instability of a viscous coflowing jet in a radial electric field," *J. Fluid Mech.* **596**, 285–311 (2008).
- ¹⁹J. M. López-Herrera, A. M. Gañón-Calvo, and M. Perez-Saborid, "One-dimensional simulation of the breakup of capillary jets of conducting liquids. Application to E.H.D. spraying," *J. Aerosol Sci.* **30**, 895–912 (1999).
- ²⁰Q. Wang, S. Mählmann, and D. T. Papageorgiou, "Dynamics of liquid jets and threads under the action of radial electric fields: Microthread formation and touchdown singularities," *Phys. Fluids* **21**, 032109-1–032109-19 (2009).
- ²¹R. T. Collins, M. T. Harris, and O. A. Basaran, "Breakup of electrified jets," *J. Fluid Mech.* **588**, 75–129 (2007).
- ²²E. R. Setiawan and S. D. Heister, "Nonlinear modeling of an infinite electrified jet," *J. Electrostat.* **42**, 243–257 (1997).
- ²³Q. Wang and D. T. Papageorgiou, "Dynamics of a viscous thread surrounded by another viscous fluid in a cylindrical tube under the action of a radial electric field: Breakup and touchdown singularities," *J. Fluid Mech.* **683**, 27–56 (2011).
- ²⁴J. M. López-Herrera and A. M. Gañón-Calvo, "A note on charged capillary jet breakup of conducting liquids: Experimental validation of a viscous one dimensional-model," *J. Fluid Mech.* **501**, 303–326 (2004).

- ²⁵ E. Georgiou, D. T. Papageorgiou, C. Maldarelli, and D. S. Rumschitzki, "The double layer-capillary stability of an annular electrolyte film surrounding a dielectric-fluid core in a tube," *J. Fluid Mech.* **226**, 149–174 (1991).
- ²⁶ D. T. Conroy, R. V. Craster, O. Matar, and D. T. Papageorgiou, "Dynamics and stability of an annular electrolyte film," *J. Fluid Mech.* **656**, 481–506 (2010).
- ²⁷ P. S. Hammond, "Nonlinear adjustment of a thin annular film of viscous fluid surrounding a thread of another within a circular cylindrical pipe," *J. Fluid Mech.* **137**, 363–384 (1983).
- ²⁸ J. R. Lister, J. Rallison, A. King, L. Cummings, and O. Jensen, "Capillary drainage of an annular film: The dynamics of collars and lobes," *J. Fluid Mech.* **552**, 311–343 (2006).
- ²⁹ D. T. Conroy, R. V. Craster, O. Matar, and D. T. Papageorgiou, "Breakup of an electrified viscous thread with charged surfactants," *Phys. Fluid* **23**, 022103-1–19 (2011).
- ³⁰ S. Kwak and C. Pozrikidis, "Effect of surfactants on the instability of a liquid thread or annular layer: Part I: Quiescent fluids," *Int. J. Multiphase Flow* **27**, 1–37 (2001).
- ³¹ L. A. Newhouse and C. Pozrikidis, "The capillary instability of annular layers and liquid threads," *J. Fluid Mech.* **242**, 193–209 (1992).
- ³² C. Pozrikidis, "Capillary instability and breakup of a viscous thread," *J. Eng. Math.* **36**, 255–275 (1999).
- ³³ C. Pozrikidis, *Boundary Integral and Singularity Method for Linearized Viscous Flow* (Cambridge University Press, New York, 1992).
- ³⁴ H. A. Stone and L. G. Leal, "The effects of surfactants on drop deformation and breakup," *J. Fluid Mech.* **220**, 161–186 (1990).
- ³⁵ W. J. Milliken, H. A. Stone, and L. G. Leal, "The effect of surfactant on the transient motion of Newtonian drops," *Phys. Fluids A* **5**, 69–79 (1993).
- ³⁶ M. Tjahjadi, H. A. Stone, and J. M. Otino, "Satellite and subsatellite formation in capillary breakup," *J. Fluid Mech.* **243**, 297–317 (1992).
- ³⁷ P. Keast and P. H. Muir, "Algorithm 688 EPDCOL: A more efficient PDECOL code," *ACM Trans. Math. Softw.* **17**, 153 (1991).
- ³⁸ R. V. Craster, O. Matar, and D. T. Papageorgiou, "Pinchoff and satellite formation in surfactant covered viscous threads," *Phys. Fluids* **14**, 1364–1376 (2002).
- ³⁹ J. Eggers and M. A. Fontelos, "The role of self-similarity in singularities of partial differential equations," *Nonlinearity* **22R**, 1–44 (2009).
- ⁴⁰ D. T. Papageorgiou, "Analytical description of the breakup of liquid jets," *J. Fluid Mech.* **301**, 109–132 (1995).